

The Maximal Gravitational Wave Signal from Asteroid-Mass Primordial Black Hole Mergers

Stefano Profumo,* Lucas Brown, and Christopher Ewasiuk

*Department of Physics, University of California,
Santa Cruz (UCSC), Santa Cruz, CA 95064, USA and
Santa Cruz Institute for Particle Physics (SCIPP), Santa Cruz, CA 95064, USA*

Sean Ricarte

*Department of Physics, University of California,
Santa Cruz (UCSC), Santa Cruz, CA 95064, USA and
Department of Physics, University of California, Merced, Merced, CA 95343, USA*

Henry Su

*Department of Physics, University of Washington, Seattle WA 98195, USA and
Department of Physics, University of Massachusetts, Amherst, MA 01003, USA*

(Dated: October 22, 2024)

Abstract

Primordial black holes can be the entirety of the dark matter in a broad, approximately five-orders-of-magnitude-wide mass range, the “asteroid mass range”, between $10^{-16} M_{\text{Sun}}$ – where constraints originate from evaporation – and $10^{-11} M_{\text{Sun}}$ – from microlensing. A direct detection in this mass range is very challenging with any known observational or experimental methods. Here we point out that, unlike previously asserted in the literature, a transient gravitational wave signal from the inspiral phase of light black hole mergers is in principle detectable with current and future high-frequency gravitational wave detectors, including but not limited to ADMX. The largest detection rates are associated with binaries from non-monochromatic mass functions in early-formed three-body systems.

* Correspondence email address: profumo@ucsc.edu

CONTENTS

I. Introduction	2
II. Constraints for a generic mass function	5
III. Microwave cavities: sensitivity	6
IV. Rate of detectable events from light black hole mergers	9
V. Comparison of different detectors and frequencies	15
VI. Discussion and Conclusions	17
Acknowledgements	19
A. Other merger pathways	19
References	20

I. INTRODUCTION

Gravitational wave (GW) observations are playing an increasingly central role in the era of multi-messenger astronomy and astrophysics as well as in the search for new physical phenomena. Interferometric detectors like LIGO/Virgo/KAGRA are sensitive to lower-frequency GWs (in the Hz to kHz range), while pulsar timing arrays are sensitive to nano-Hertz frequencies [1]. At the opposite end of the GW spectrum, high-frequency GWs (HFGWs) require radically novel detection approaches [2]. Broadly, the field of HFGWs, specifically at frequencies in the megahertz and above, is a rapidly developing area of research with significant theoretical challenges and technical hurdles (see e.g. Ref. [3] for a recent overview).

The experimental landscape of HFGW detectors includes mechanical resonators [4], such as resonant spheres, levitated sensor detectors, and bulk acoustic wave devices, broadly operating in the few kHz up to GHz frequencies; devices hinging on the so-called inverse Gertsenshtein effect [5], involving the conversion of gravitons into photons, such as superconducting radio-frequency cavities, resonant antennas, and conversion of GWs into electromagnetic waves in the presence of

a static magnetic field, as in axion search experiments and axion helioscopes, and resonant LC circuits [6] – broadly sensitive to frequencies between MHz and GHz; interferometers, such as the HOL experiment, and other techniques, including for instance using the frequency modulation of photons in laser beams or employing superconducting circuits [7].

A staggering feature of HFGWs is the purported absence of known astrophysical backgrounds, making a detection a potent signal of new physics or of a new class of GW sources. In this study we focus on one specific source of HFGW: light, nearby primordial black hole (PBH) mergers. PBHs – BHs of non-stellar origin formed, for instance, from large density fluctuations, on the scale of the cosmic event horizon, in the early universe – continue to attract growing attention; PBHs could be a large fraction or, depending on their mass, the totality of the Universe’s dark matter; be responsible for the production of the dark matter itself, or the matter-antimatter asymmetry in the universe [8]; produce observed anomalous gamma-ray and cosmic-ray signals [9, 10]; and provide a window into otherwise utterly secluded dark sectors [11, 12]. The detection of PBH mergers could shed light on early Universe conditions, and on the question of the microscopic nature of the cosmological dark matter (we point the reader to recent reviews on these and related topics, such as Ref. [13, 14]).

PBH mergers are not the exclusive potential source of HFGWs. Other exotic phenomena include cosmic strings, oscillons, and scenarios involving early Universe dynamics such as inflation (e.g., quintessential inflationary models) [15, 16]. These sources might produce HFGWs during different early Universe processes, including in certain baryogenesis scenarios [15]. PBH evaporation could also source very HFGWs [2], with recently-proposed possible cosmological realizations leading to lower-frequency signals than those traditionally expected at or near the Planck scale [17, 18]. Some speculative models involve high-energy particle interactions or nuclear processes that might generate detectable GWs at these high frequencies and, broadly, HFGWs offer a new window to test models extending beyond the Standard Model, including those involving extra dimensions or modifications to gravity [19].

HFGW from light PBH mergers has been explored in a number of more or less recent studies. Ref. [20] explores the energy density of relic GWs from PBH mergers; Ref. [21] discusses MHz-GHz GWs related to PBHs and baryogenesis; Ref. [22] considers the stochastic background of high-frequency GWs from early PBH mergers; Ref. [23] explores evaporated PBHs and associated GWs; Ref. [24] examines PBH binary production and GW merger rates. Ref. [25] investigates

PBH mergers and induced secondary GWs using inflationary models; Ref. [26] analyzes stochastic background from curvature fluctuations; [27] reviews PBH binary formation and merger theories; Ref. [28] offers end-to-end analyses of PBH GW signatures; [29] critiques detection prospects for sub-solar PBHs; [30] calculates merger rates and evaluates mass distributions related to PBHs; [31] discusses inflationary PBHs and resulting GWs; Ref. [32] connects LIGO observations to PBH-induced GWs from cosmic inflation.

In the present study, we illustrate how, contrary to claims made in some of the studies above, even current generation axion search experiments, such as ADMX, could in principle be sensitive to up to several tens of light PBH merger events per year, under the most optimistic-possible conditions, motivating the study of archival data to search for the associated signals¹. The conditions that would enable a significant event rate include (i) considerable clustering at early times, leading to enhanced early binary formation, (ii) a large over-abundance of dark matter locally, (iii) a non-monochromatic PBH mass function, and (iv) a PBH mass abundance close to the totality of the cosmological dark matter abundance. Additionally, as we will describe, such large event rates only occur in a relatively narrow PBH mass range, between 10^{-13} and 10^{-11} solar masses. Somewhat intriguingly, within such mass range PBHs can possibly constitute the totality of the cosmological dark matter, and are especially challenging to detect, escaping microlensing searches and evaporation constraints [14].

The remainder of this study is structured as follows: in the next section II we describe the formalism and constraints on PBH populations of non-monochromatic mass functions; the ensuing sec. III outlines and discusses the sensitivity of microwave cavities to HFGWs specifically originating from PBH mergers, including with non-monochromatic mass functions; sec. IV then focuses on the most significant pathway leading to the largest merger event rate, and on the corresponding rate of detectable events at an ADMX-like microwave cavity – we leave it to the Appendix to present a comparison to other possible pathways, leading to considerably subdominant event rates; the final sec. VI then presents our discussion and conclusions.

¹ This search is at present ongoing with the ADMX Collaboration.

II. CONSTRAINTS FOR A GENERIC MASS FUNCTION

We consider a mass distribution of PBHs (the so-called “mass function”), the mass-weighted differential number of PBHs, of the standard form

$$\psi(m) \equiv \frac{1}{m} \frac{dn_{\text{PBH}}(m)}{dm}, \quad (1)$$

normalized so that the cosmological mass density of PBHs ρ_{PBH} relative to the cosmological dark matter abundance ρ_{DM}

$$f_{\text{PBH}} = \int \psi(m) dm. \quad (2)$$

We refer to monochromatic mass functions, corresponding to the form

$$\psi_0(m) = f_{\text{PBH}}(m_0) \delta(m - m_0), \quad (3)$$

and to “dichromatic” mass functions,

$$\psi_{\text{DC}}(m) = f_1 \delta(m - m_1) + f_2 \delta(m - m_2). \quad (4)$$

The latter is especially well motivated in the present context, as previous studies have numerically shown that the structure of mass functions that maximize black hole merger rates are generally rather close to the schematic form in Eq. (4) (see e.g. Ref. [33]).

Note that translating from the customarily shown constraints on monochromatic mass functions, representing the largest-possible value of $f_{\text{PBH}}^{\text{max}}(m_0)$ for Eq. (3) above compatible with experimental and observational constraints, to a generic mass function $\psi(m)$ amounts to requiring that [34]

$$\int \frac{\psi(m)}{f_{\text{PBH}}^{\text{max}}(m)} dm \leq 1. \quad (5)$$

Hence, the resulting constraint on f_1 and f_2 for a monochromatic mass function is (dropping the superscript “max” from now on):

$$\frac{f_1}{f_{\text{PBH}}(m_1)} + \frac{f_2}{f_{\text{PBH}}(m_2)} \leq 1. \quad (6)$$

For a given f_1 , the value of f_2 that maximizes the mass-density of PBHs is then fixed by

$$f_2 = \text{Max} \left(f_{\text{PBH}}(m_2) \left(1 - \frac{f_1}{f_{\text{PBH}}(m_1)} \right), 0 \right) = \text{Max} \left(\frac{f_{\text{PBH}}(m_2)}{f_{\text{PBH}}(m_1)} (f_{\text{PBH}}(m_1) - f_1), 0 \right). \quad (7)$$

III. MICROWAVE CAVITIES: SENSITIVITY

Resonant cavities – first proposed to search for axions [35] – are sensitive to high-frequency GWs: a GW passing in a cavity endowed with a static magnetic field sources an effective electromagnetic current that, in turn, generates an electromagnetic field at the same frequency of the GW [36–39]. Currently-operating and proposed detectors include ADMX [40–42], HAYSTAC [43], CAPP [44], and ORGAN [45]. Here, for definiteness, we consider an ADMX-type detector for our estimates. In particular, we adopt the following estimate for ADMX’s sensitivity to the GW amplitude [46]:

$$h_0^{\text{sens}} = 3 \times 10^{-22} \left(\frac{0.1}{\eta_n} \right) \left(\frac{8 \text{ T}}{|\vec{B}|} \right) \left(\frac{0.1 \text{ m}^3}{V_{\text{cav}}} \right)^{5/6} \left(\frac{10^5}{Q} \right)^{1/2} \left(\frac{T_{\text{sys}}}{1 \text{ K}} \right)^{1/2} \left(\frac{1 \text{ GHz}}{\nu} \right)^{3/2} \left(\frac{\Delta\nu}{10 \text{ kHz}} \right)^{1/4} \left(\frac{1 \text{ min}}{\Delta t} \right)^{1/4}. \quad (8)$$

In the equation above, η_n is the cavity’s effective GW coupling; Note that in the most-optimal possible case, i.e. when the azimuthal direction of the relevant cavity mode resonates with the spin structure of the gravitational field, the cavity’s effective coupling coefficient η_n is $\mathcal{O}(0.1)$ [36]. This includes the TM_{010} and TM_{020} modes in use for axion experiments like ADMX. It was also found in [39] that $\eta_n \approx 0.14$ for the TM_{012} mode. Note that while [46] presents the coupling coefficient as $\mathcal{O}(1)$, the authors used $\eta_n = 0.1$ in their calculations for the strain sensitivities of ADMX and SQMS. We use the same here, albeit with future optimization this may actually be an under-estimate.

Also in Eq. (8), $|\vec{B}|$ is the cavity’s magnetic field; Q is the quality factor of the cavity; ν the operating resonant frequency; and $\Delta\nu \sim \nu/Q$ the bandwidth. The other parameters are the cavity’s volume, operating temperature, and acquisition observation time. Unless otherwise specified, we will utilize the pivot values in Eq. (8) as our reference values for the sensitivity of an ADMX-like microwave cavity.

As customary, we define the chirp mass of the binary as

$$m_c \equiv \frac{(m_1 m_2)^{3/5}}{(m_1 + m_2)^{1/5}}. \quad (9)$$

The characteristic strain signal of the GW amplitude at a frequency ν reads [1]

$$h_c^{\text{sig}}(m_c, \nu, d) = \nu |\tilde{h}(\nu)| = \frac{1}{\pi^{2/3}} \left(\frac{5}{24} \right)^{1/2} \frac{c}{d} \left(\frac{G m_c}{c^3} \right)^{5/6} \left(\frac{1}{\nu} \right)^{1/6} \quad (10)$$

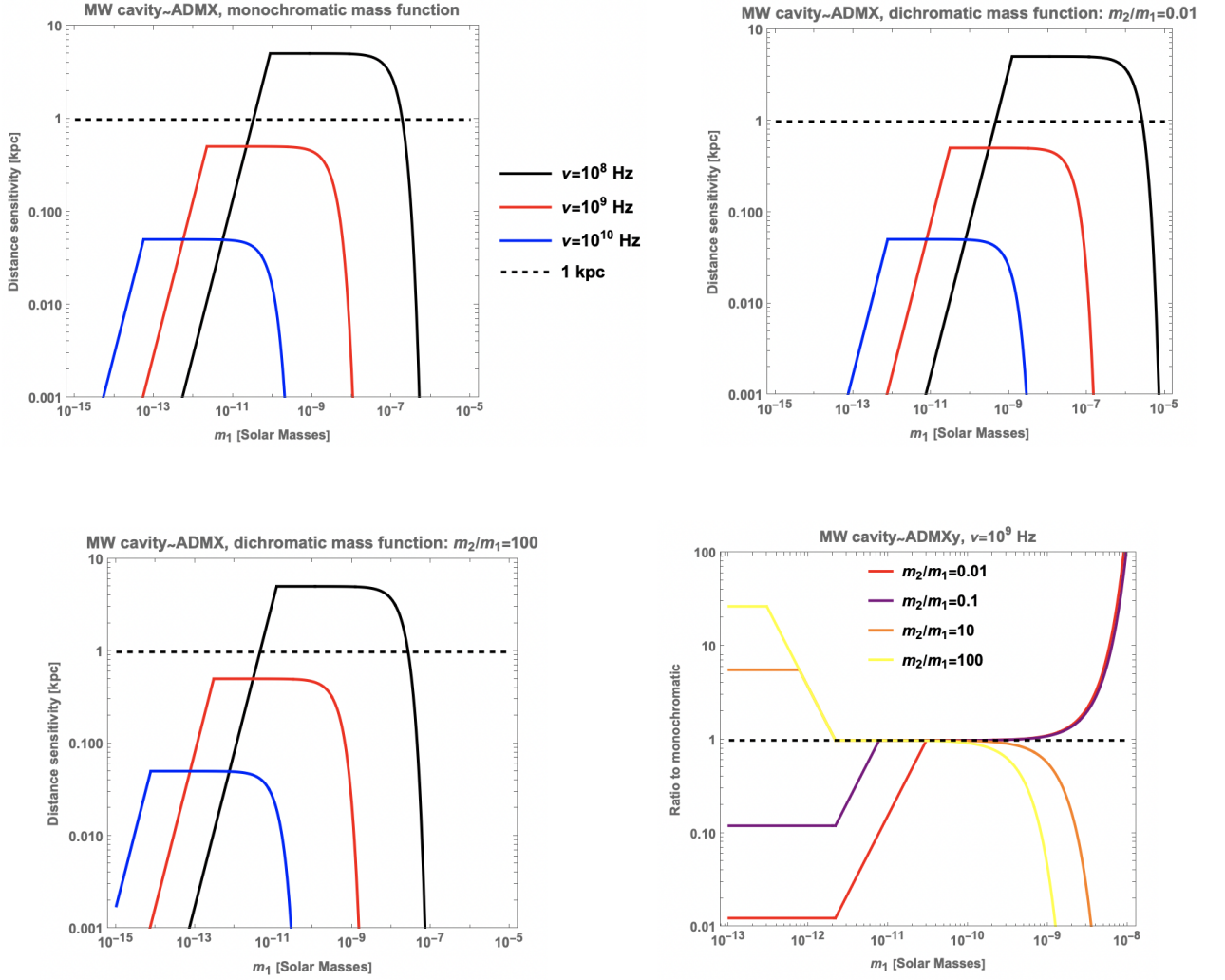


Figure 1. Distance sensitivity comparison for a microwave cavity with specifications close to ADMX's for three different frequencies, $\nu = 10^8$, 10^9 and 10^{10} Hz. In the top left corner we assume a monochromatic mass function, in the top right that $m_2/m_1 = 10^{-2}$, in the bottom left that $m_2/m_1 = 10^2$; in the bottom right we instead show the ratio, for $\nu = 10^9$ Hz, of the distance sensitivity for a given mass ratio m_2/m_1 as in the legend, divided by that for the monochromatic case, $m_1 = m_2$

for a merger at distance d with chirp mass m_c . Standard GW theory of binaries gives, for the duration of the signal around a frequency ν [1],

$$\tau(m_c, \nu) = \frac{5}{256} (\pi\nu)^{-8/3} \left(\frac{Gm_c}{c^3} \right)^{-5/3}. \quad (11)$$

At a detector with observation time Δt and bandwidth $\Delta\nu$, the signal additionally depends on the number of cycles observed N_{cycles} ; the latter, in turn, depends on the time of variation

of the frequency of the signal (i.e. how long the signal effectively spends at a given frequency) $t_\nu = \nu/\dot{\nu}$, the ring-up time of the cavity, corresponding to the inverse of the cavity bandwidth, and the duration of the signal via

$$h_c^{\text{sig,det}}(m_c, \nu, d) = h_c^{\text{sig}}(m_c, \nu, d) \sqrt{N_{\text{cycles}}} \text{Min}[1, \Delta t/t_\nu] \exp(-\tau(\nu)\Delta\nu), \quad (12)$$

where we have assumed as usual that the ring-up effect is exponential. In the expression above, the number of cycles

$$N_{\text{cycles}} = \int_{t_{\text{min}}}^{t_{\text{max}}} \dot{\nu} dt = \int_{\nu_{\text{min}}}^{\nu_{\text{max}}} d\nu \frac{\nu}{\dot{\nu}} \simeq \frac{\nu^2}{\dot{\nu}}, \quad (13)$$

the derivative of frequency is

$$\dot{\nu} = \frac{96}{5} \pi^{8/3} \left(\frac{Gm_c}{c^3} \right)^{5/3} \nu^{11/3}, \quad (14)$$

and the characteristic time spent at a frequency ν is

$$t_\nu(m_c, \nu) = \frac{\nu}{\dot{\nu}}. \quad (15)$$

Therefore, a merger is visible to a detector with characteristic strain sensitivity h_c^{sens} out to a distance

$$d_{\text{sens}}(m_1, m_2, \nu) = \frac{\sqrt{N_{\text{cycles}}} \text{Min}[1, \Delta t/t_\nu] \exp(-\tau(\nu)\Delta\nu)}{h_c^{\text{sens}}} \frac{c}{\pi^{2/3}} \left(\frac{5}{24} \right)^{1/2} \left(\frac{Gm_c}{c^3} \right)^{5/6} \left(\frac{1}{\nu} \right)^{1/6}. \quad (16)$$

We show the ADMX distance sensitivity at a frequency ν for mergers involving two masses m_1 and m_2 in Fig. 1. The top left panel shows the monochromatic mass function case, $m_1 = m_2$ for three different frequencies, $\nu = 10^8$, 10^9 and 10^{10} Hz, while the top right panel assumes a dichromatic mass function of mass ratio $m_1/m_2 = 0.01$ and the bottom left panel of $m_1/m_2 = 0.01$, again for the same three frequencies. Note that the shape of the curves as a function of mass reflects the mass dependence of the sensitivity function $d_{\text{sens}}(m_1, m_2, \nu)$; as a function of mass at fixed frequency, the function exhibits three regimes

1. at small masses, i.e. for $t_\nu > \Delta t$, corresponding to, approximately $m_{\text{PBH}} < 10^{-10} M_{\text{Sun}} (10^8 \text{ Hz}/\nu)$, the critical distance depends on the product $(\sqrt{N_{\text{cycles}}}/t_\nu) h_c^{\text{sig}} \sim m^{-5/6} m^{5/3} m^{5/6} \sim m^{5/3}$
2. at intermediate masses, for $(1/\Delta\nu < t_\nu < \Delta t)$, the critical distance depends on the product $(\sqrt{N_{\text{cycles}}}) h_c^{\text{sig}} \sim m^{-5/6} m^{5/6}$ and is thus mass-independent;

3. finally, for $t_\nu < 1/\Delta\nu$ the critical distance is exponentially suppressed by the ring-up time of the cavity being much larger than the time the signal spends at frequency ν .

Similar considerations elucidate the frequency dependence shown in the figures.

In the bottom right panel of Fig. 1 we show, for $\nu = 10^9$ Hz, the ratio of the distance sensitivity for a given mass ratio m_2/m_1 to that corresponding to a monochromatic mass function ($m_1 = m_2$), as a function of m_1 . The plot illustrates how mass function ratios, $m_2/m_1 < 1$, can be detected at a greater distance than the monochromatic case, due to presence of lighter binaries that can ring up the cavity for larger values of m_1 ; vice-versa, for high mass function ratios, $m_2/m_1 > 1$ the presence of *heavier* pairs makes part of the signal brighter and thus detectable at a further distance. We note that in any case *a non-monochromatic mass function generically enables larger distance sensitivities than the monochromatic case*, for sufficiently spaced-out masses.

IV. RATE OF DETECTABLE EVENTS FROM LIGHT BLACK HOLE MERGERS

In what follows we are concerned with the calculation of the rate of detectable events from light PBH mergers, principally with a monochromatic or dichromatic mass function, at a microwave resonant cavity such as ADMX.

For a generic mass function $\psi(m)$, the *rate* of visible mergers at frequency ν , for a detector whose critical distance sensitivity is given by the function $d_{\text{sens}}(m_1, m_2, \nu)$ in Eq. (16), reads

$$R[\psi](f) = \int_{m_{\min}}^{\infty} dm_1 \int_{m_{\min}}^{\infty} dm_2 \frac{dR[\psi](f)}{dm_1 dm_2} \frac{4\pi}{3} d_{\text{sens}}^3(m_1, m_2, f), \quad (17)$$

where m_{\min} corresponds to black holes long-lived enough not to have expired yet, the upper limit of integration is controlled by the exponential in Eq. (12), and R is the merger rate for the given mass function and frequency.

We demonstrate in the Appendix that the largest differential merger rate today corresponds to the early three-body binary formation pathway (*E3* in what follows), discussed in detail in Ref. [47] (see their Eq. (2.13)):

$$\begin{aligned} \frac{dR_{E3}}{dm_1 dm_2 dm_3} &= \frac{9}{296\pi} \frac{1}{\tilde{\tau}} \left(\frac{t_0}{\tilde{\tau}} \right)^{-34/37} \left(\Gamma \left[\frac{58}{37}, \tilde{N} \left(\frac{t_0}{\tilde{\tau}} \right)^{3/16} \right] - \Gamma \left[\frac{58}{37}, \tilde{N} \left(\frac{t_0}{\tilde{\tau}} \right)^{-1/7} \right] \right) \\ &\quad \times \tilde{x}^{-3} \delta_{\text{dc}}^{-1} \tilde{N}^{53/37} \bar{m}^3 \frac{\psi(m_1)}{m_1} \frac{\psi(m_2)}{m_2} \frac{\psi(m_3)}{m_3}. \end{aligned} \quad (18)$$

In the equation above (restoring factors of c suppressed in the original reference),

$$\tilde{\tau} \equiv c^5 \frac{384 \alpha^4 \beta^7 a_{\text{eq}}^4 m_3^7 \tilde{x}^4}{85 G^3 \eta M^{10}}, \quad (19)$$

where we will hereafter assume $\alpha = \beta = 1$,

$$\eta \equiv \frac{m_1 m_2}{M^2}, \quad M \equiv m_1 + m_2, \quad (20)$$

and

$$\tilde{x}^3 \equiv \frac{3}{4\pi} \frac{M}{a_{\text{eq}}^3 \rho_{\text{eq}}}. \quad (21)$$

Finally,

$$\tilde{N} \equiv \delta_{\text{dc}} \Omega_{\text{DM,eq}} \frac{M}{\bar{m}}, \quad \text{and} \quad \bar{m} \equiv \left(\int dm \frac{\psi(m)}{m} \right)^{-1}. \quad (22)$$

In the expressions above, the matter-radiation equality corresponds to the energy density relative to the critical density, and expansion factor

$$\Omega_{\text{eq}} = 0.4, \quad \text{with} \quad a_{\text{eq}} \simeq 1/3400. \quad (23)$$

A crucial input to the expressions above is the local density contrast δ_{dc} at the decoupling redshift corresponding to

$$a_{\text{dc}} \approx a_{\text{eq}} \left(\frac{x}{\tilde{x}} \right)^3, \quad (24)$$

where $x \equiv r/a$ is the comoving distance. Assuming that the PBH two-point function $\xi(x)$ is constant at comoving distances smaller than \tilde{x} specified above in Eq. (21), i.e.

$$1 + \xi(x) \approx \delta_{\text{dc}} \quad \text{for} \quad x < \tilde{x}, \quad (25)$$

strong clustering corresponds to $\delta_{\text{dc}} \gg 1$ [47]. Following Ref. [46] and [48], in order to assess the maximal-possible merger rate we additionally consider a large local enhancement factor $\delta_{\text{local}} \sim 2 \times 10^5$, linearly impacting the merger rate $R \rightarrow \delta_{\text{local}} R$, reflecting the fact that the merger rate is sensitive to the *local* dark matter density – i.e. assuming that the binary density follows the dark matter density.

We note that the expression above can be *maximized* by expanding the Gamma function in the asymptotically large δ_{dc} limit, by using the asymptotic expansion for the incomplete Gamma function

$$\Gamma[a, z] \simeq e^{-z} z^{a-1} \quad z \rightarrow \infty. \quad (26)$$

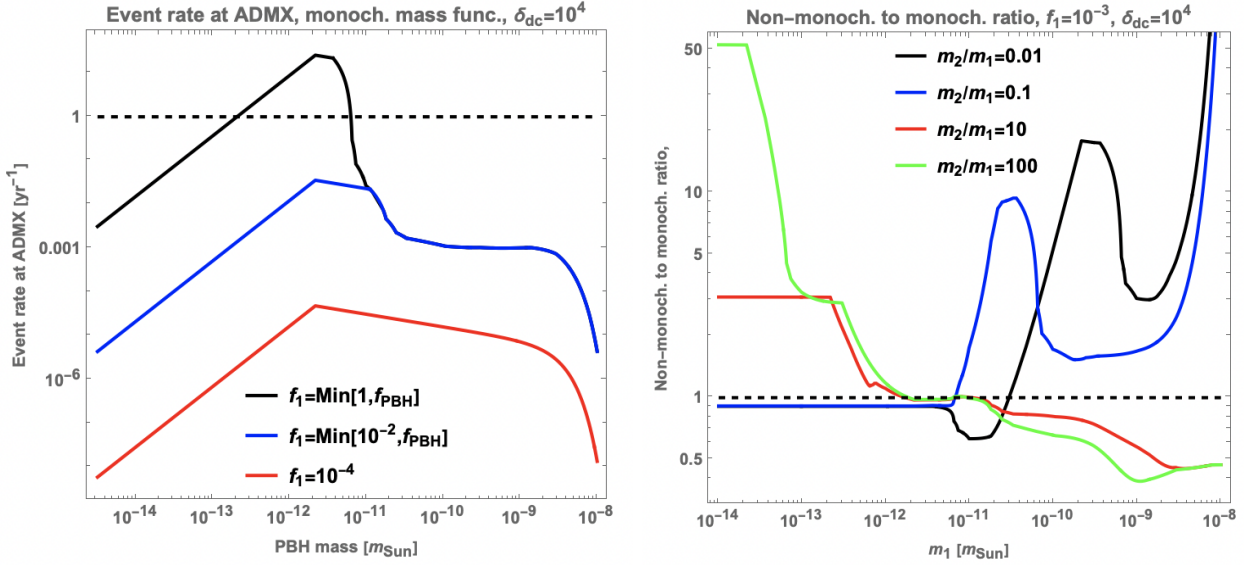


Figure 2. Left: rates (in events per year) for a monochromatic mass function with a fixed mass fraction f_1 (if $f_1 > f_{\text{PBH}}$, i.e. when the assumed mass fraction violates observational limits, we set the mass fraction to its maximal possible value $f = f_{\text{PBH}}$). Right: the ratio, as a function of m_1 , of event rates for dichromatic mass functions with a given $0.01 \leq m_2/m_1 \leq 100$, to the monochromatic case, for $f_1 = 10^{-3}$ and for $\delta_{\text{dc}} = 10^4$

Neglecting the second Gamma function, which is very suppressed compared to the first one for large values of the second argument, one obtains

$$\frac{dR_{E3}}{dm_1 dm_2 dm_3} = \frac{9}{296\pi} \frac{1}{\tilde{\tau}} \left(\frac{t_0}{\tilde{\tau}}\right)^{-13/16} \left(\exp \left[-\tilde{N} \left(\frac{t_0}{\tilde{\tau}}\right)^{3/16} \right] \right) \tilde{N}^2 \times \tilde{x}^{-3} \delta_{\text{dc}}^{-1} \bar{m}^3 \frac{\psi(m_1)}{m_1} \frac{\psi(m_2)}{m_2} \frac{\psi(m_3)}{m_3}. \quad (27)$$

We will not use the expression above, which is, however, relevant to interpret our numerical results below.

Fig. 2, left, shows the merger rates for a monochromatic mass function with a fixed mass fraction f (if $f > f_{\text{PBH}}$, i.e. when the assumed mass fraction violates observational limits, we set the mass fraction to its maximal possible value $f = f_{\text{PBH}}$). The peak occurs at masses where (i) the constraints on f_{PBH} allow PBH to be the entirety of the dark matter, and (ii) the distance sensitivity plateaus at its maximal value, for the frequency under consideration.

The right panel of fig. 2 shows the ratio, as a function of m_1 of event rates for dichromatic

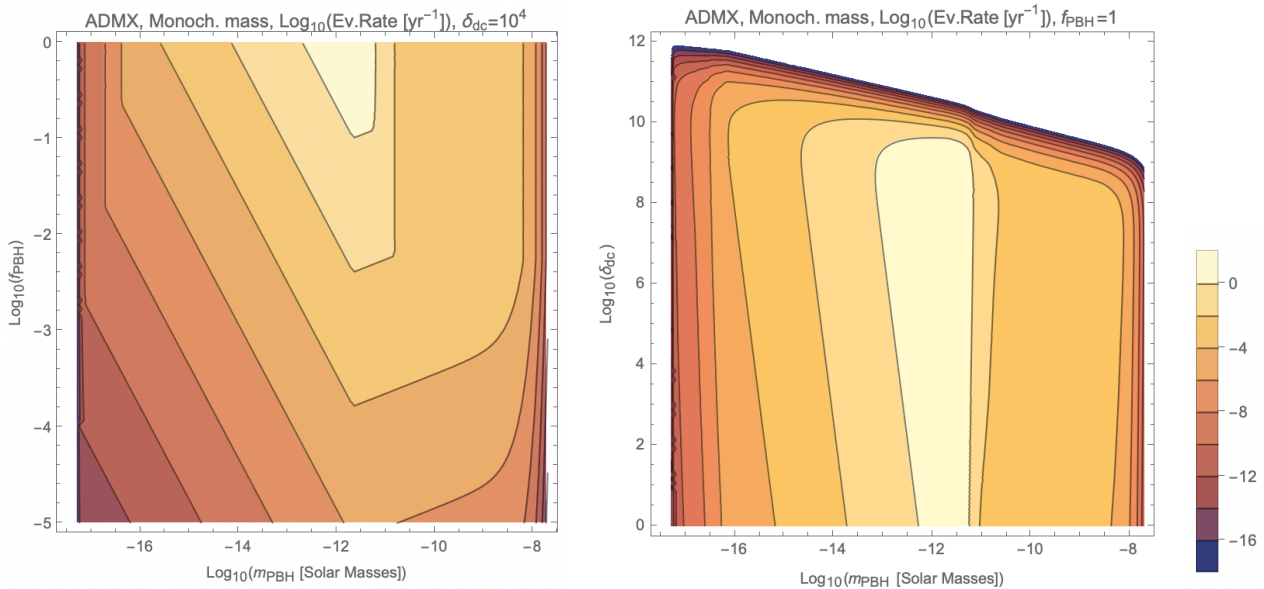


Figure 3. Contours of constant Log_{10} of the event rate per year for a putative ADMX-like cavity for a monochromatic mass function varying the binary merger mass m_{PBH} and f_{PBH} with $\delta_{\text{dc}} = 10^4$ (left), and varying instead δ_{dc} with $f = \min(f_{\text{PBH}}, 1)$

mass functions with a given $0.01 \leq m_2/m_1 \leq 100$, to the monochromatic case, for $f_1 = 10^{-3}$ and for $\delta_{\text{dc}} = 10^4$ (this latter parameter is largely uninfluential here). As noted above for the bottom, right panel of fig. 1, when $m_2/m_1 > 1$ larger mass binaries enhance the visibility of the signal compared to the monochromatic case, especially at low masses; a non-trivial peak, which could be larger than an order of magnitude, appears instead at low mass fractions $m_2/m_1 < 1$, a non-trivial combination of the larger sensitivity distance shown in fig. 1 and of the declining sensitivity at high masses due to both constraints on f_{PBH} and the exponential suppression from the rung-up cavity time constraint.

The contour plots in fig. 3 show, on a Log_{10} scale, the event rate per year for a putative ADMX-like cavity for a monochromatic mass function varying the binary merger mass and f_{PBH} (left) with $\delta_{\text{dc}} = 10^4$ (left), and varying instead δ_{dc} with $f = \min(f_{\text{PBH}}, 1)$. The sharp decrease at the extreme left and right edges of the plots are related to increasingly tight constraints on the abundance of PBH at that mass; we also note that the region with several events per year extends over a relatively conspicuous range of masses, $10^{-13} \lesssim m_{\text{PBH}}/m_{\text{Sun}} \lesssim 10^{-11}$, and down to PBH densities of about 10% of the dark matter density; additionally, the right panel highlights

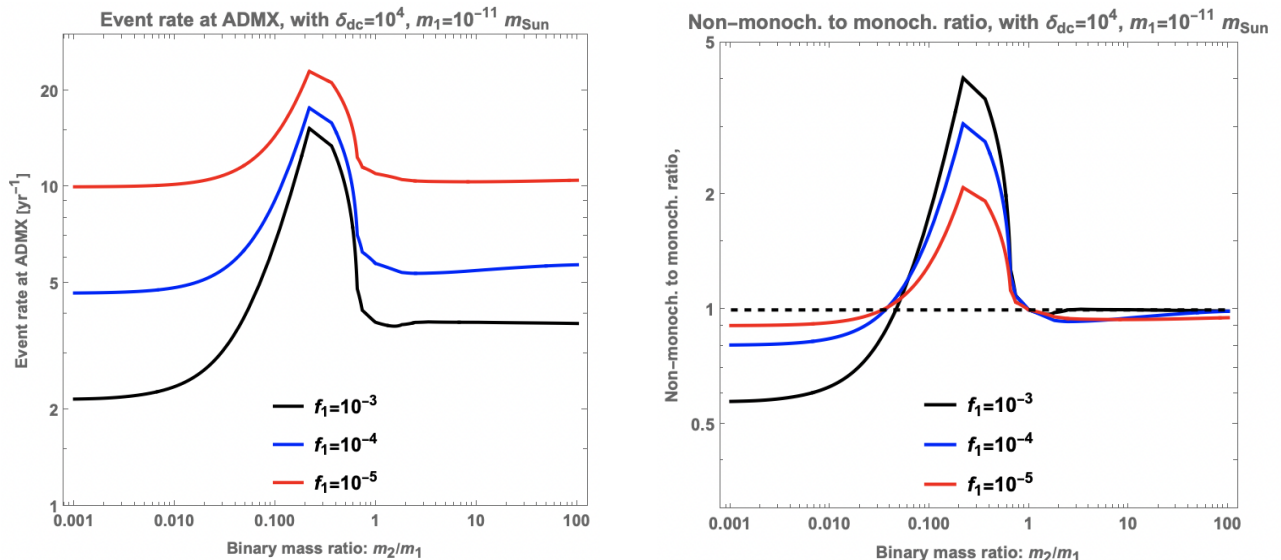


Figure 4. Left: Event rate at an ADMX-like cavity for different $f_1 = 10^{-3}$, 10^{-4} , 10^{-5} as a function of the binary mass ratio m_2/m_1 , with $m_1 = 10^{-11} m_{Sun}$, for $\delta_{dc} = 10^4$. Right: same as in the left panel, but as a ratio to the monochromatic $m_2 = m_1$ rate

the relatively weak dependence of the event rate on δ_{dc} outside of the exponential suppression at $\delta_{dc} \gtrsim 10^9$, noted already e.g. in [46].

Fig. 4 relaxes the assumption of a monochromatic mass function, and considers, for three different values of the “weight” f_1 of the first mass m_1 (see Eq.(4)), the event rate as a function of the mass ratio m_2/m_1 . Note that here and hereafter we assume the maximal f_2 , fixed by Eq. 7 (for $f_1 \leq_{PBH}(m_1)$, otherwise the curves are interrupted as the abundance exceeds limits). In the figure, we assume $m_1 = 10^{-11} m_{Sun}$, for $\delta_{dc} = 10^4$. The right panel shows the same, but as a ratio to the monochromatic $m_2 = m_1$ case, and highlights how a non-monochromatic mass ratio predicts, for m_2 between $0.05m_1$ and $0.9m_1$, a larger event rate than the monochromatic case.

Fig. 5 studies the effect of clustering, but for a dichromatic mass function, varying a number of parameters, and as a function of the clustering parameter, δ_{dc} . Both panels assume $m_1 = 10^{-11} m_{Sun}$; in the left panel we fix $f_1 = 0.01$ and vary the mass ratio $m_2/m_1 = 0.1, 1, 10$; in the right panel we fix, instead, $m_2/m_1 = 0.01$, and vary $f_1 = 0.01, 1$ and 10^{-4} . As usual, f_2 is maximized for a given f_1 , as per Eq. (7).

The main takeaway point in this figure is that the event rate is only rather weakly dependent on early clustering, although the effect can be as large as one order of magnitude. Additionally,

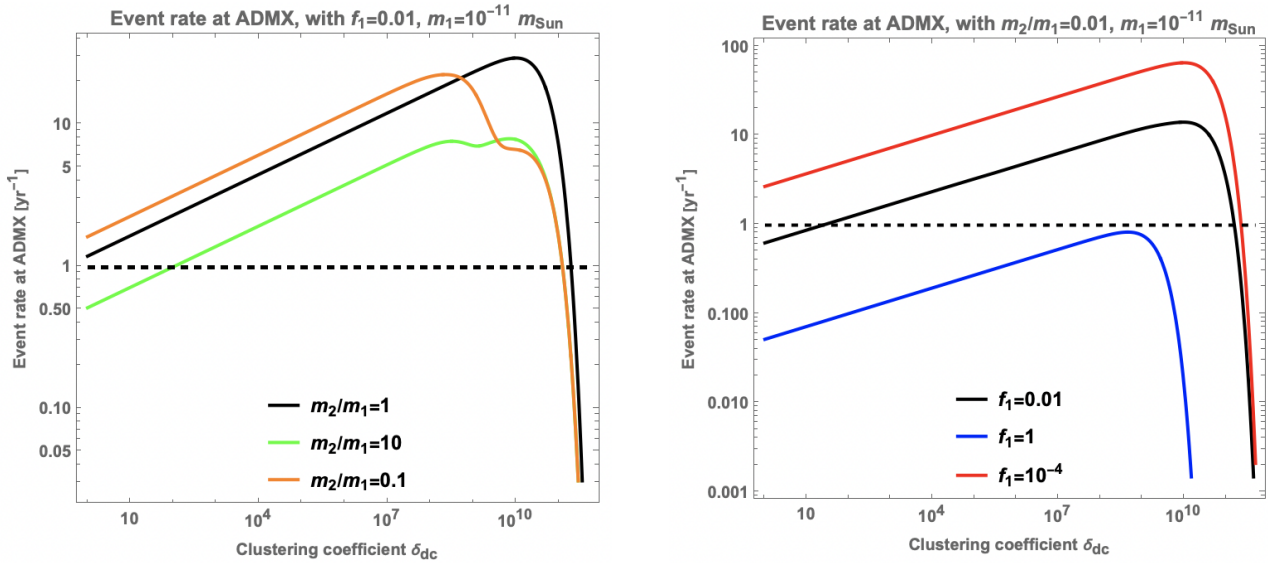


Figure 5. The dependence of the event rate per year on the clustering coefficient δ_{dc} , for three different mass ratios $m_2/m_1 = 1, 10, 0.1$ with $f_1 = 0.01$ and $m_1 = 10^{-11} m_{\text{Sun}}$ (left) and for three different values of $f_1 = 0.01, 1, 10^{-4}$

the effect rather strongly depends on the mass ratio for a non-monochromatic mass function. Also, notably, at very large clustering there exists an exponential suppression, deriving from the physical effect that mergers in this case have already occurred at very early times and the binaries thus have been exhausted.

The contour plots of fig. 6 illustrate, as above on a Log10 scale, but different color-coding, the event rate on the planes defined by the mass ratio m_2/m_1 versus clustering coefficient δ_{dc} (left) and f_1 (right). In both plots we fix $m_1 = 10^{-11} m_{\text{Sun}}$, while we set $f_1 = 10^{-5}$ in the left panel and $\delta_{\text{dc}} = 10^4$ in the right panel. Note that as in previous plots, f_2 is maximized for a given f_1 . Also notice that in the white regions in the right panel, $f_1 > f_{\text{PBH}}(m_1)$. The white regions in the left panel, instead, have vanishingly small event rates because of the exponential suppression discussed above.

The left panel highlights that the maximal rate, approximately independent of m_2/m_1 , is achieved for $10^5 \lesssim \delta_{\text{dc}} \lesssim 10^9$, with relatively little numerical differences across that range. The right panel, instead, shows how the event rate has a relatively mild dependence on the mass ratio, except at large f_1 , where larger rates correspond to mass ratio not too far (within an order of magnitude or so) from unity.

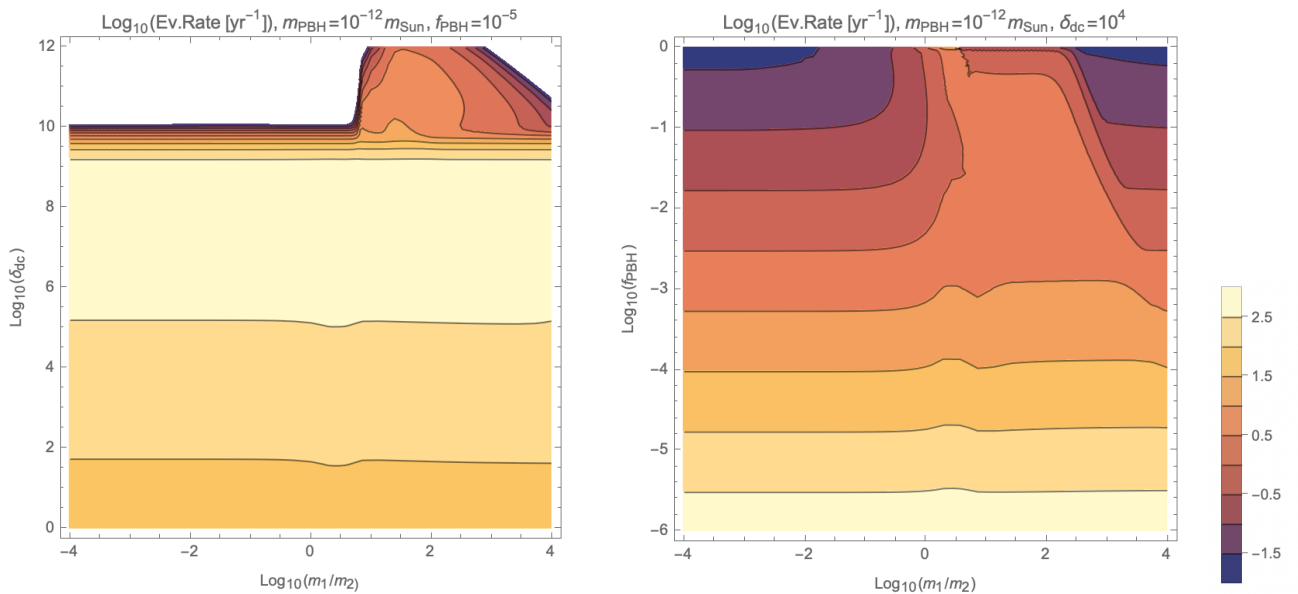


Figure 6. Contour plots of the Log₁₀ of the event rate per year as a function of the dichromatic mass function ratio m_2/m_1 , for $m_1 = 10^{-12} m_{\text{Sun}}$, versus δ_{dc} with $f_1 = 10^{-5}$ (and maximized f_2) (left) and f_1 (right) with $\delta_{\text{dc}} = 10^4$.

In the final four panels of fig. 7 we study the event rate, on the plane defined by the masses in the merging binary m_1 and m_2 . In all panels we fix $\delta_{\text{dc}} = 10^4$, and, clockwise from the top left, we set $f_1 = 10^{-1}$, 10^{-3} , 10^{-5} and 10^{-10} . The white regions correspond to $f_1 > f_{\text{PBH}}(m_1)$.

In all cases, we find that rates are largest in the range around $10^{-13} \lesssim m_{1,2}/m_{\text{Sun}} \lesssim 10^{-13}$, with peaks at values slightly in excess of $10^{-12} m_{\text{Sun}}$. The details of each panel are interesting and straightforward to interpret based on the discussion of the plots above. Note that the color range is not the same for all plots, and that the event rate is increasingly large with decreasing f_1 .

V. COMPARISON OF DIFFERENT DETECTORS AND FREQUENCIES

We compare, here, the rates expected with improved, future detectors, sensitive to a broader range of frequencies. Specifically, we consider a version of ADMX with a significantly reduced resonant frequency of $\nu = 0.65$ GHz (corresponding to ADMX run1A; note that for instance the recent run1D is around 1.4GHz), with all other parameters set to the default values indicated above. For all detectors we assume 60 seconds integration times.

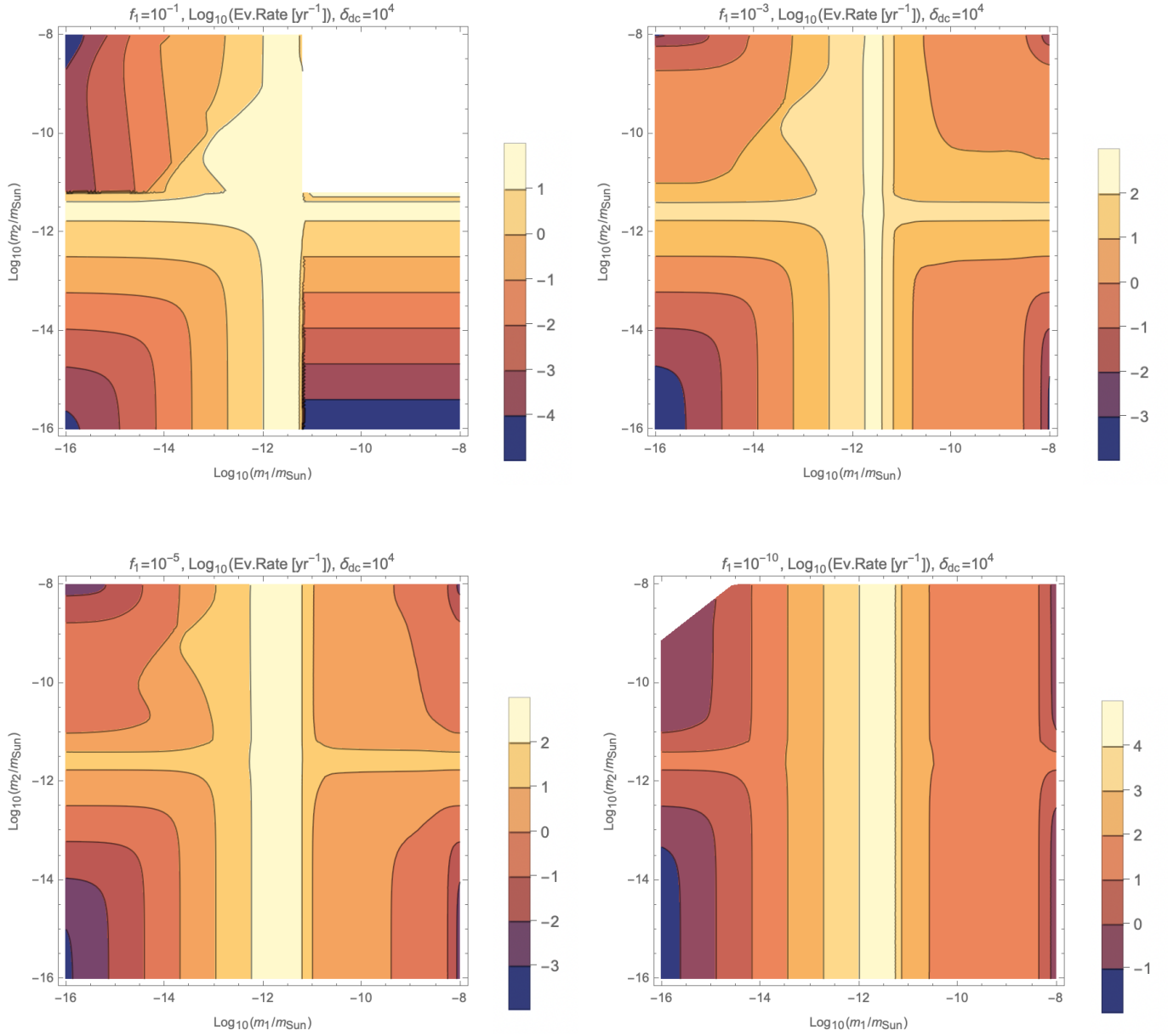


Figure 7. Four panels showing the Log_{10} contours for the yearly event rate on the (m_1, m_2) plane, all at $\delta_{\text{dc}} = 10^4$, for $f_1 = 10^{-1}, 10^{-3}, 10^{-5}, 10^{-10}$ in clockwise order from the top left

For the SQMS detector we employed the parameters indicated in Ref. [49]: $f \in (1 - 2)$ GHz, $Q \sim 10^6$, $|\mathbf{B}| = 5$ T, $V_{\text{cav}} = 100$ L, $T_{\text{sys}} = 1$ K, and $\eta_n = 0.1$ as for ADMX.

For the ADMX-EFR we utilize projections provided by the ADMX Collaboration², featuring a magnetic field – 9.4 T at central field (mean over cavities on the order of 9.1 T), a cavity

² G.P. Carosi, private communication

volume consisting of an 18 cavity array with combined volume of approximately 218 liters in the frequency range 2-3 GHz and 182 liters (3-4 GHz), and a Cavity Unloaded Quality factor of 120k; the total system noise temperature was assumed to be 440 mK.

Finally - albeit the geometric structure of the detector may pose non-trivial coupling differences from the linear structure of ADMX - for DM Radio GUT we assume the parameters given in³ and also outlined in [6] (assuming the sensitivity is approximately reflected in our Eq.(8) above): a magnetic field of 16 T, a volume of 4,580 L, a quality factor of 10^6 , a system noise temperature of 1 mK, and a frequency of 4 GHz.

We present a comparison of the expected, maximal yearly event rate with these various setups in fig. 8. Generally, as expected, higher frequencies of operation extend the detectors sensitivity to lower masses, and increase the range of masses where a significant event rate should occur (see especially the right panel). The scaling of detectors performance in terms of the detector parameters is otherwise clearly evident from the expression in Eq. (8).

We note that given the large local overdensity assumed here, which, once again, produces *maximal* expected event rates, we predict that ADMX-EFR could see up to 100 events; however, neglecting the overdensity enhancement, this rate would be significantly lower. Even without a larger local overdensity, however, DM Radio GUT is expected to see a few events over its lifetime.

VI. DISCUSSION AND CONCLUSIONS

The realization that a number of devices originally conceived for different experimental purposes could be used in the quest for high-frequency GWs has spurred a resurgent interest in potential signals. Parallel to this, as the search for weakly-interacting particle dark matter dawns [50, 51] with no compelling evidence of it being realized in nature has also given rise to renewed interest in primordial black holes as dark matter candidates. Interestingly, a broad black hole mass range, between, approximately, masses of 10^{-16} and 10^{-10} solar masses (the “asteroid mass range”) is compatible with these objects being the entirety of the cosmological, and Galactic, dark matter.

The asteroid mass window is, however, extremely complicated to probe. At low masses, evaporation via Hawking-Bekenstein radiation is too slow; at high masses microlensing is not effective

³ <https://indico.fnal.gov/event/63051/>

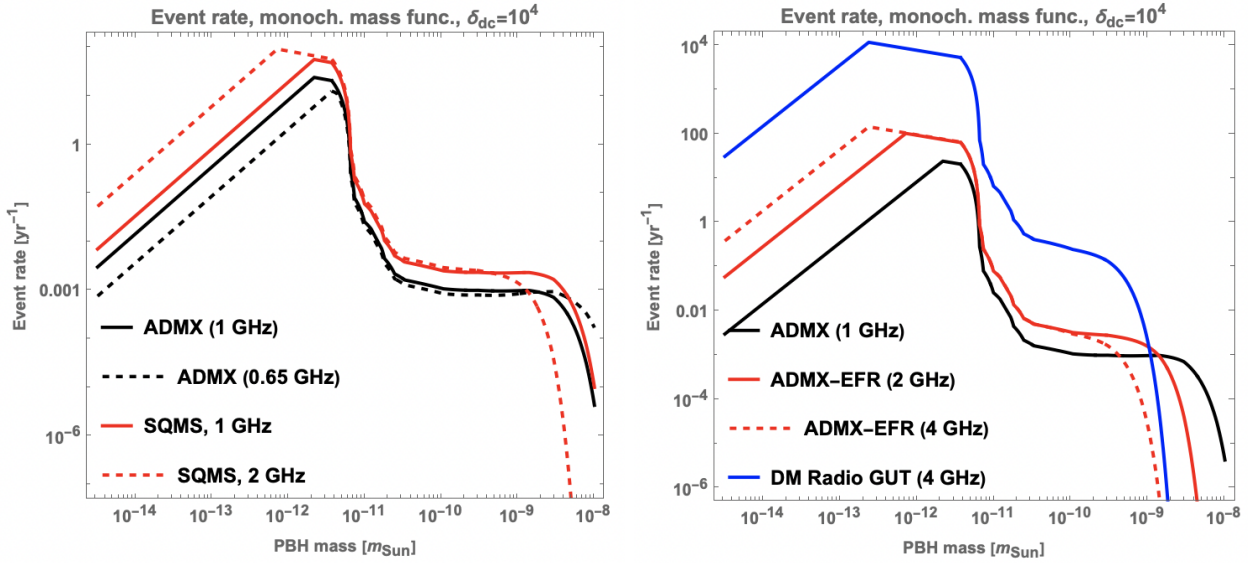


Figure 8. Left: A comparison of the yearly event rate at different frequencies for ADMX (1 and 0.65 GHz) and for SQMS (1 and 2 GHz); Right: The same as in the left panel, but for ADMX-EFR at 2 and 4 GHz, and for DM Radio GUT at 4 GHz

because of a number of technical reasons related to finite size source effects, wave optics, and the interplay of event duration and observational cadence. However, mergers of such light black holes could give rise to GHz frequency gravitational waves signals similar to those detected, at much lower frequency, by the interferometers LIGO/Virgo/KAGRA, and potentially detectable by the above-mentioned re-purposed detectors.

Here, we provide an in-depth examination and proof of principle of the discovery potential of experiments similar to the microwave resonant cavity ADMX to light, asteroid-mass primordial black hole mergers. Our assumptions are purposely optimistic, stretching the event rates to their maximal possible values. This includes maximizing the effect of clustering upon binary formation, the local density of Galactic dark matter, and the black hole mass function, the latter being customarily and systematically assumed to be monochromatic in previous studies (see e.g. [6, 39, 46]).

We found that even current-generation ADMX-like cavities could, in principle, be sensitive to *hundreds* of merger events, with future detectors enhancing these rates by further factors up to 100. We find that, again in the most optimistic-possible case, the distance sensitivity to mergers extends up to several kpc for current-generation cavities, and much further for future

detectors, with the best sensitivity to masses right in the middle of the asteroid mass range, around $10^{-12}m_{\text{Sun}}$.

This study addressed closely the role of a non-monochromatic mass function, showing that event rates can be enhanced by orders of magnitude compared to the usually-assumed monochromatic case; everywhere, we took into consideration the relevant observational constraints on the black hole abundance, as they apply to non-trivial mass functions. We first assessed the most significant pathway to binary formation, and concluded that throughout the parameter space of interest it is associated with early, three-body binary formation. We then studied how event rates depend on a “dichromatic” mass function - one that features two subpopulations of different masses in different proportions, which has been shown elsewhere to maximize the merger event rate [33]. We also studied the effect of clustering at early (and late) times, and prospects for current and future detectors alike.

We hope our results will spur the utilization of archival data to search for the expected transient events for all detectors relevant for this scope. The discovery of a high-frequency GW merger would be momentous, shaking the fields of astrophysics and particle physics alike, and ushering a new era in the quest for the nature of the cosmological dark matter.

ACKNOWLEDGEMENTS

We thank Chelsea Bartram, Nick Du, Gray Rybka and Gianpaolo Carosi for input, feedback, and discussions. This work is partly supported by the U.S. Department of Energy grant number de-sc0010107 (SP).

Appendix A: Other merger pathways

In [52] the authors presented an update of their previous work [47] on early three-body mergers. Albeit an improvement in several aspects of the calculation, this latter discussion does not include a detailed discussion of the effect of early-time clustering. We verified that the differences in the merger rate compared to Ref. [47] are actually marginal and within a factor of a few, when $\delta_{\text{dc}} = 1$. As such, we resort to the expression discussed above.

Other merger pathways include the early two-body (E2), late two-body (L2), and late three-

body (L3) formation scenarios. For a generic mass function ψ , the E2 pathway merger rate for masses m_1, m_2 reads [52]

$$\frac{dR_{E2}}{dm_1 dm_2} \approx \frac{1.6 \times 10^6}{\text{Gpc}^3 \text{ yr}} f_{\text{PBH}}^{\frac{53}{37}} \eta^{-\frac{34}{37}} \left(-\frac{32}{37}\right)^{-\frac{32}{37}} S_L S_E \frac{\psi(m_1)}{m_1} \frac{\psi(m_2)}{m_2} \quad (\text{A1})$$

where as usual $f_{\text{PBH}} = \int \psi(m) dm$, $\eta = m_1 m_2 / (m_1 + m_2)^2$, $M = m_1 + m_2$, and S_L and S_E are suppression factors (which for the sake of comparison with the E3 rate we set to 1 below).

The late, 2-body pathway leads to a merger rate [52]

$$\frac{dR_{E2}}{dm_1 dm_2} \approx \frac{3.4 \times 10^{-6}}{\text{Gpc}^3 \text{ yr}} f_{\text{PBH}}^2 \delta_{\text{eff}} \left(\frac{\sigma_v}{\text{km/s}}\right)^{-\frac{11}{7}} \eta^{-\frac{5}{7}} \frac{\psi(m_1)}{m_1} \frac{\psi(m_2)}{m_2}, \quad (\text{A2})$$

where δ_{eff} is a local DM density contrast factor, and we assume a local velocity dispersion $\sigma_v \sim 100$ km/s.

Finally, the 3-body late mergers reads [52]

$$\frac{dR_{L3}}{dm_1 dm_2} \approx \frac{1.3 \times 10^{-16} e^{-6.0(\gamma-1)}}{\text{Gpc}^3 \text{ yr}} f_{\text{PBH}}^3 \delta_{\text{eff}}^2 \left(\frac{\sigma_v}{\text{km/s}}\right)^{-9+\frac{8\gamma}{7}} \eta^{-1+\frac{\gamma}{7}} \tilde{\mathcal{F}} \left(\frac{\langle m \rangle}{2\eta M} \kappa_{\text{min}}\right) \frac{\psi(m_1)}{m_1} \frac{\psi(m_2)}{m_2},$$

where the function $\tilde{\mathcal{F}}$ is detailed in Ref. [52], and $1 < \gamma < 2$, which determines the initial angular momentum distribution of the binaries,

$$\frac{dP}{dj} \sim \gamma j^{\gamma-1},$$

is assumed to be 1.1 (we find that the induced uncertainty from varying γ is mild).

We compare the four pathways first, for simplicity, using a monochromatic mass function in the left panel of Fig. 9. We assume a density contrast $\delta_{\text{dc}} = 10^4$ for all pathways (we implement it as described at the end of Ref. [52] for the pathways E2, L2 and L3) and we use for each mass the maximal possible value of $f_{\text{PBH}}(m_{\text{PBH}}$ for a given mass. The figure shows that the E3 pathway dominates everywhere between 6 and 7 orders of magnitude to the next most significant pathway.

The right panel of fig. 9 shows the results for a dichromatic mass function, with the mass function mass ratio m_2/m_1 shown in the x axis. Here again it is fully apparent how the E3 pathway dominates other pathways by several orders of magnitude, justifying in full the approach we take in this analysis.

[1] Michele Maggiore. *Gravitational Waves. Vol. 1: Theory and Experiments*. Oxford University Press, 2007.

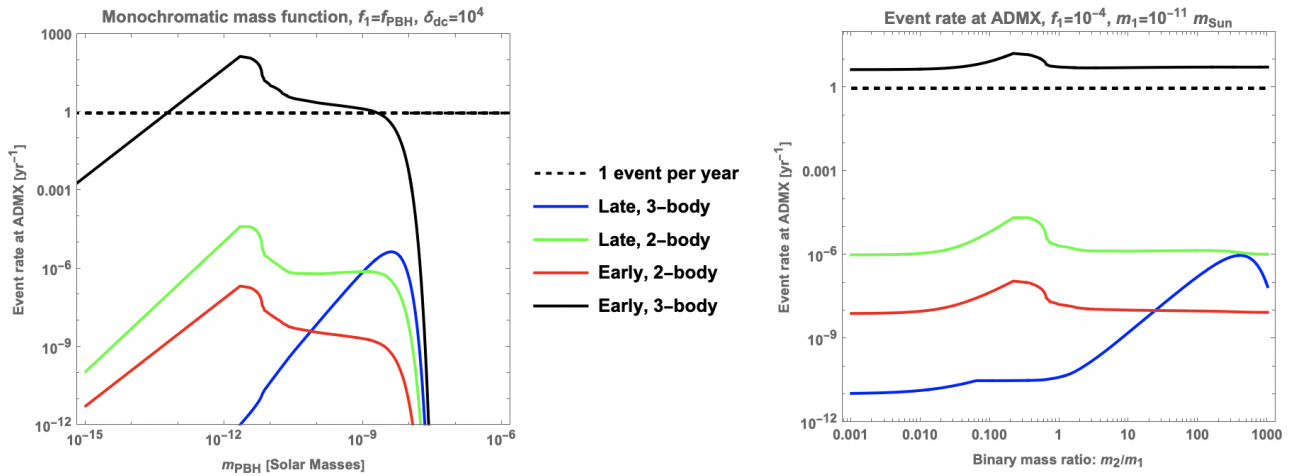


Figure 9. Pathways comparison – see the text for details.

- [2] Alexander D. Dolgov and Damian Ejlili. Relic gravitational waves from light primordial black holes. *Phys. Rev. D*, 84:024028, 2011.
- [3] Massimo Giovannini. Relic gravitons and high-frequency detectors. *JCAP*, 05:056, 2023.
- [4] Gregory M. Harry, Thomas R. Stevenson, and Ho Jung Paik. Detectability of gravitational wave events by spherical resonant mass antennas. *Phys. Rev. D*, 54:2409–2420, 1996.
- [5] Andrea Palessandro and Tony Rothman. A simple derivation of the Gertsenshtein effect. *Phys. Dark Univ.*, 40:101187, 2023.
- [6] Valerie Domcke, Camilo Garcia-Cely, and Nicholas L. Rodd. Novel Search for High-Frequency Gravitational Waves with Low-Mass Axion Haloscopes. *Phys. Rev. Lett.*, 129(4):041101, 2022.
- [7] Torsten Bringmann, Valerie Domcke, Elina Fuchs, and Joachim Kopp. High-frequency gravitational wave detection via optical frequency modulation. *Phys. Rev. D*, 108(6):L061303, 2023.
- [8] Logan Morrison, Stefano Profumo, and Yan Yu. Melanopogenesis: Dark Matter of (almost) any Mass and Baryonic Matter from the Evaporation of Primordial Black Holes weighing a Ton (or less). *JCAP*, 05:005, 2019.
- [9] Zachary S. C. Picker and Alexander Kusenko. Explaining the GeV excess with exploding black holes. *Phys. Lett. B*, 845:138175, 2023.
- [10] Mrunal Korwar and Stefano Profumo. Late-forming black holes and the antiproton, gamma-ray, and anti-helium excesses. 3 2024.
- [11] Michael J. Baker and Andrea Thamm. Probing the particle spectrum of nature with evaporating

- black holes. *SciPost Phys.*, 12(5):150, 2022.
- [12] Michael J. Baker and Andrea Thamm. Black hole evaporation beyond the Standard Model of particle physics. *JHEP*, 01:063, 2023.
- [13] Bernard Carr and Florian Kuhnel. Primordial Black Holes as Dark Matter: Recent Developments. *Ann. Rev. Nucl. Part. Sci.*, 70:355–394, 2020.
- [14] Albert Escrivà, Florian Kuhnel, and Yuichiro Tada. Primordial Black Holes. 11 2022.
- [15] Thomas C. Gehrman, Barmak Shams Es Haghi, K. Sinha, and Tao Xu. Baryogenesis, primordial black holes and mhz–ghz gravitational waves, 2022.
- [16] Fang yu Li, Meng xi Tang, and D. Shi. Electromagnetic response of a gaussian beam to high frequency relic gravitational waves in quintessential inflationary models, 2003.
- [17] Aurora Ireland, Stefano Profumo, and Jordan Scharnhorst. Primordial gravitational waves from black hole evaporation in standard and nonstandard cosmologies. *Phys. Rev. D*, 107(10):104021, 2023.
- [18] Aurora Ireland, Stefano Profumo, and Jordan Scharnhorst. Gravitational waves from primordial black hole evaporation with large extra dimensions. *JCAP*, 08:033, 2024.
- [19] Thomas C. Gehrman, Barmak Shams Es Haghi, K. Sinha, and Tao Xu. The primordial black holes that disappeared: connections to dark matter and mhz-ghz gravitational waves, 2023.
- [20] A. Dolgov and Damian Ejlli. Relic gravitational waves from light primordial black holes, 2011.
- [21] Thomas C. Gehrman, Barmak Shams Es Haghi, K. Sinha, and Tao Xu. Baryogenesis, primordial black holes and mhz,Àighz gravitational waves, 2022.
- [22] D. Hooper, G. Krnjaic, J. March-Russell, Samuel D. McDermott, and R. Petrossian-Byrne. Hot gravitons and gravitational waves from kerr black holes in the early universe., 2020.
- [23] Thomas C. Gehrman, Barmak Shams Es Haghi, K. Sinha, and Tao Xu. The primordial black holes that disappeared: connections to dark matter and mhz-ghz gravitational waves, 2023.
- [24] M. Raidal, V. Vaskonen, and H. Veermae. Gravitational waves from primordial black hole mergers, 2017.
- [25] Zhu Yi, Qing Gao, Y. Gong, and Zong hong Zhu. Primordial black holes and secondary gravitational waves from inflationary model with a non-canonical kinetic term, 2020.
- [26] Juan Garcia-Bellido, Marco Peloso, and Caner Unal. Gravitational Wave signatures of inflationary models from Primordial Black Hole Dark Matter. *JCAP*, 09:013, 2017.

- [27] Martti Raidal, V. Vaskonen, and H. Veermae. Formation of primordial black hole binaries and their merger rates, 2024.
- [28] E. Bagui, S. Clesse, V. D. Luca, J. Ezquiaga, G. Franciolini, J. Garc'ia-Bellido, Cristian Joana, R. K. Jain, S. Kuroyanagi, I. Musco, T. Papanikolaou, A. Raccanelli, S. Renaux-Petel, A. Riotto, E. R. Morales, M. Scalisi, O. Sergijenko, C. Unal, V. Vennin, and David Wands. Primordial black holes and their gravitational-wave signatures, 2023.
- [29] G. Franciolini, Anshuman Maharana, and F. Muia. Hunt for light primordial black hole dark matter with ultrahigh-frequency gravitational waves, 2022.
- [30] Andrew D. Gow, C. Byrnes, A. Hall, and J. Peacock. Primordial black hole merger rates: distributions for multiple ligo observables, 2019.
- [31] Antonino Cangialosi. Cosmological constraints on primordial black holes, 2019.
- [32] Keisuke Inomata, M. Kawasaki, K. Mukaida, Y. Tada, and T. Yanagida. Inflationary primordial black holes for the ligo gravitational wave events and pulsar timing array experiments, 2016.
- [33] Benjamin V. Lehmann, Stefano Profumo, and Jackson Yant. Model-independent discovery prospects for primordial black holes at LIGO. *Mon. Not. Roy. Astron. Soc.*, 501(3):3727–3740, 2021.
- [34] Bernard Carr, Martti Raidal, Tommi Tenkanen, Ville Vaskonen, and Hardi Veermäe. Primordial black hole constraints for extended mass functions. *Phys. Rev. D*, 96(2):023514, 2017.
- [35] P. Sikivie. Experimental Tests of the Invisible Axion. *Phys. Rev. Lett.*, 51:1415–1417, 1983. [Erratum: *Phys.Rev.Lett.* 52, 695 (1984)].
- [36] Asher Berlin, Diego Blas, Raffaele Tito D’Agnolo, Sebastian A. R. Ellis, Roni Harnik, Yonatan Kahn, and Jan Schütte-Engel. Detecting high-frequency gravitational waves with microwave cavities. *Phys. Rev. D*, 105(11):116011, 2022.
- [37] Valerie Domcke, Camilo Garcia-Cely, and Nicholas L. Rodd. Novel Search for High-Frequency Gravitational Waves with Low-Mass Axion Haloscopes. *Phys. Rev. Lett.*, 129(4):041101, 2022.
- [38] Asher Berlin et al. Searches for New Particles, Dark Matter, and Gravitational Waves with SRF Cavities. 3 2022.
- [39] Claudio Gatti, Luca Visinelli, and Michael Zantedeschi. Cavity detection of gravitational waves: Where do we stand? *Phys. Rev. D*, 110(2):023018, 2024.
- [40] C. Boutan et al. Piezoelectrically Tuned Multimode Cavity Search for Axion Dark Matter. *Phys. Rev. Lett.*, 121(26):261302, 2018.

- [41] T. Braine et al. Extended Search for the Invisible Axion with the Axion Dark Matter Experiment. *Phys. Rev. Lett.*, 124(10):101303, 2020.
- [42] C. Bartram et al. Search for Invisible Axion Dark Matter in the 3.3–4.2 μeV Mass Range. *Phys. Rev. Lett.*, 127(26):261803, 2021.
- [43] L. Zhong et al. Results from phase 1 of the HAYSTAC microwave cavity axion experiment. *Phys. Rev. D*, 97(9):092001, 2018.
- [44] S. Lee, S. Ahn, J. Choi, B. R. Ko, and Y. K. Semertzidis. Axion Dark Matter Search around 6.7 μeV . *Phys. Rev. Lett.*, 124(10):101802, 2020.
- [45] Ben T. McAllister, Graeme Flower, Justin Kruger, Eugene N. Ivanov, Maxim Goryachev, Jeremy Bourhill, and Michael E. Tobar. The ORGAN Experiment: An axion haloscope above 15 GHz. *Phys. Dark Univ.*, 18:67–72, 2017.
- [46] Gabriele Franciolini, Anshuman Maharana, and Francesco Muia. Hunt for light primordial black hole dark matter with ultrahigh-frequency gravitational waves. *Phys. Rev. D*, 106(10):103520, 2022.
- [47] Martti Raidal, Ville Vaskonen, and Hardi Veermae. Gravitational Waves from Primordial Black Hole Mergers. *JCAP*, 09:037, 2017.
- [48] Oriol Pujolas, Ville Vaskonen, and Hardi Veermae. Prospects for probing gravitational waves from primordial black hole binaries. *Phys. Rev. D*, 104(8):083521, 2021.
- [49] Asher Berlin, Diego Blas, Raffaele Tito D’Agnolo, Sebastian A. R. Ellis, Roni Harnik, Yonatan Kahn, and Jan Schütte-Engel. Detecting high-frequency gravitational waves with microwave cavities. *Phys. Rev. D*, 105(11):116011, 2022.
- [50] Giorgio Arcadi, Maíra Dutra, Pradipta Ghosh, Manfred Lindner, Yann Mambrini, Mathias Pierre, Stefano Profumo, and Farinaldo S. Queiroz. The waning of the WIMP? A review of models, searches, and constraints. *Eur. Phys. J. C*, 78(3):203, 2018.
- [51] Giorgio Arcadi, David Cabo-Almeida, Maíra Dutra, Pradipta Ghosh, Manfred Lindner, Yann Mambrini, Jacinto P. Neto, Mathias Pierre, Stefano Profumo, and Farinaldo S. Queiroz. The Waning of the WIMP: Endgame? 3 2024.
- [52] Martti Raidal, Ville Vaskonen, and Hardi Veermae. Formation of primordial black hole binaries and their merger rates. 4 2024.